Contents lists available at ScienceDirect

Materials Science & Engineering A

journal homepage: www.elsevier.com/locate/msea

Revealing the ultra-high high-temperature compressive mechanical properties and deformation mechanism of a heterostructured AlN$_p$/Al nanocomposite

Mengqi Jiang [a,1], Yuli Wu [a,1], Jinfeng Nie [a,*], Yuyao Chen [a], Yong Fan [a], Xiangfa Liu [b], Yonghao Zhao [a,**]

[a] Nano and Heterogeneous Materials Center, School of Materials Science and Engineering, Nanjing University of Science and Technology, Nanjing, 210094, China
[b] Key Laboratory for Liquid–Solid Structural Evolution and Processing of Materials, Ministry of Education, Shandong University, Jinan, 250061, China

ARTICLE INFO

ABSTRACT

Heterostructured materials have attracted increasing attention owing to their superior mechanical properties. In this work, the high-temperature mechanical property and deformation mechanism of a heterostructured AlN$_p$/Al composite were revealed by isothermal compression tests. The results showed that the superior compressive strength of the AlN$_p$/Al composite could be maintained at both room temperature and high temperature of 300–500 °C during the whole deformation process. The strong pinning effect of the dispersive AlN nanoparticle (AlN$_p$) on the matrix grains could prevent grain boundary softening and grain growth, as well as the special layered heterogeneous structure and network structure could avoid high temperature softening. The hot deformation mechanism of the AlN$_p$/Al composite could be affected by the strain rate and deformation temperature. It was confirmed that continuous dynamic recrystallization (CDRX) dominated the whole deformation process when deformed at low strain rates (0.0001–0.01 s^{-1}) and high temperatures (400–500 °C); while dynamic recovery (DRV) was the main mechanism at high strain rate (0.1–1 s^{-1}) and low temperature (300–350 °C) Furthermore, the strain rate sensitivity exponent (m) was used to assess the relationship between peak stress and deformation temperature and strain rate, which could predict the instability region of the composite. It shows that the simultaneous action of high temperatures and high strain rates should be avoided during hot deformation. This work shed light on the microstructure design of the high-strength heat-resistant aluminum matrix composite.

1. Introduction

With the development of various fields towards lightweight, modernization, and high speed, the requirements for high performance alloys with lightweight, high strength and high toughness are growing [1–3]. In recent years, the tendency of "aluminum instead of steel" has attracted increasing attention, and many researchers have shifted the focus to high-strength aluminum alloys. Compared with traditional aluminum alloys, particle reinforced aluminum matrix composites (PRAMCs) are expected to become a kind of promising materials for industrial development because of the advantages of both the matrix metals and reinforcing particles, such as low density, high strength, good corrosion resistance and high elastic modulus [4–6]. Many studies revealed that PRAMCs exhibited better mechanical properties than single aluminum alloys. Yi et al. [7]. prepared submicron-sized TiC reinforced Al-4.5Cu composites, which showed significantly improved strength and ductility compared with cast Al–Cu alloys. The 0.5TiC/Al–Cu composite had the best tensile properties with a 43% increase in ultimate tensile strength (UTS), a 31% increase in yield strength (YS) and a 142% increase in elongation. Yan et al. [8]. introduced Si$_3$N$_4$ particles into 2026Al by gravity casting and hot extrusion. It was found that the nano-AlN particles transition layer on the surface of the Si$_3$N$_4$ particles has good interfacial bonding with the Al matrix, which resulted in better tensile properties than the matrix alloy.

---

* Corresponding author.
** Corresponding author.
 E-mail addresses: niejinfeng@njust.edu.cn (J. Nie), yhzhao@njust.edu.cn (Y. Zhao).
[1] These authors contributed equally to this work.
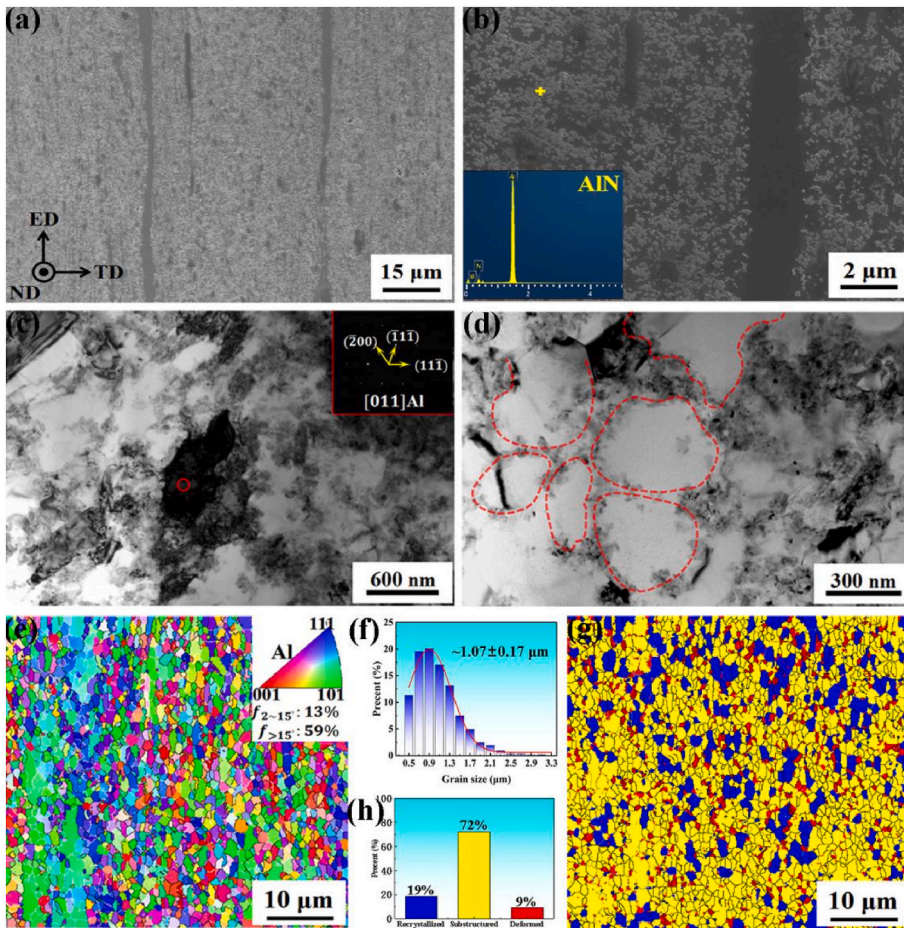
Fig. 1. Microstructure images of the extruded AlN_p/Al composite before compression: (a)–(b) SEM images and EDS; (c) a low magnification TEM image, and the corresponding SAD pattern; (d) a magnified TEM image showing the distribution of the AlN particles; (e) the crystal orientation map, and the inset is the IPF color code; (f) grain size distribution; (g) recrystallized distribution (blue is the recrystallized grain, yellow is the substructure grain, red is the deformed grain); (h)fraction of various types of grains. (For interpretation of the references to color in this figure legend, the reader is referred to the Web version of this article.)

Generally, in addition to inherent excellent properties, PRAMCs are often subjected to heat treatment or hot deformation processes to regulate the microstructure, thereby precipitating nanoscale second phase or building heterogeneous structures to further enhance performance. Tang et al. [9] introduced stainless steel particles synergistically reinforced 6061Al with SiC particles. The ductility was improved without losing strength and the overall properties were greatly improved after ageing. Nie et al. [10]. used hot rolling to form a non-uniform grain structure in the Al matrix, thus inducing additional HDI strengthening and hardening to further enhance the properties of $Al_3BC/6061Al$. However, the high temperature deformation behavior of the material is complex and variable during the hot deformation process. The appearance of phenomena such as work hardening, dynamic recovery (DRV), and dynamic recrystallization (DRX) can lead to the evolution of the material microstructure, which significantly affect the material properties [11,12]. On the other hand, the high strain hardening rate and poor ductility due to the influence of particle-reinforced lead to reduced plastic deformation ability [13]. Furthermore, microstructure evolutions and property changes during the hot deformation process are mainly controlled by the deformation parameters. Therefore, it is greatly important to study the high-temperature mechanical behavior and deformation mechanism of PRAMCs and to reveal the optimal hot processing range to understand the hot processability of the composite.

However, in addition to the UTS and YS during high temperature deformation, researchers are now focusing more on creep and thermal stability [14–17]. With the increasing complexity and versatility of the applications put forward higher demands on the high temperature properties, such as aircraft landing gear, drilling rods of deep well, and aluminum tubes in oilfield, all of which require consideration of high

temperature compression properties, especially compression strength. Compared with other PRAMCs, AlN_p/Al composites have better high-temperature tensile and creep resistance [18], but there are few studies on the deformation behaviour and the corresponding deformation mechanism during the hot compression process.

In this work, a 12.3% AlN_p/Al composite was prepared by in-situ synthesis method and isothermal compression tests were carried out on the 12.3% AlN_p/Al composite under different temperatures and strain rates. The high temperature compressive strength, microstructure evolution and the corresponding deformation mechanisms of the composite were investigated. In addition, the constitutive equations and hot processing maps of the composite were established, which showed the optimum hot processing process range. This work provided guidance for the design of high strength heat-resistant aluminum matrix materials.

2. Experimental

The 12.3% AlN_p/Al composite was fabricated by liquid-solid reaction combined with the subsequent extrusion process [19], which was labeled as "as-extruded" (all compositions quoted in this work are in wt. % unless otherwise stated). The raw materials are commercial pure Al powders (99.7%), nitrogen plasmids powders (98.5%) and active carbon powders (99.0%) supplied by Shandong Al&Mg Melt Technology Co. Ltd. (Jinan, China).

All samples used for characterization were taken from the central part of the cylindrical compressed samples. The microstructures of the samples were characterized by a field emission scanning electron microscope (FESEM, Quanta 250F, FEI, Hillsboro, OR, USA) equipped with an energy dispersive spectroscopy (EDS, Oxford Instruments, Oxford, UK), electron backscatter diffraction (EBSD) with a FIB/SEM dual-beam
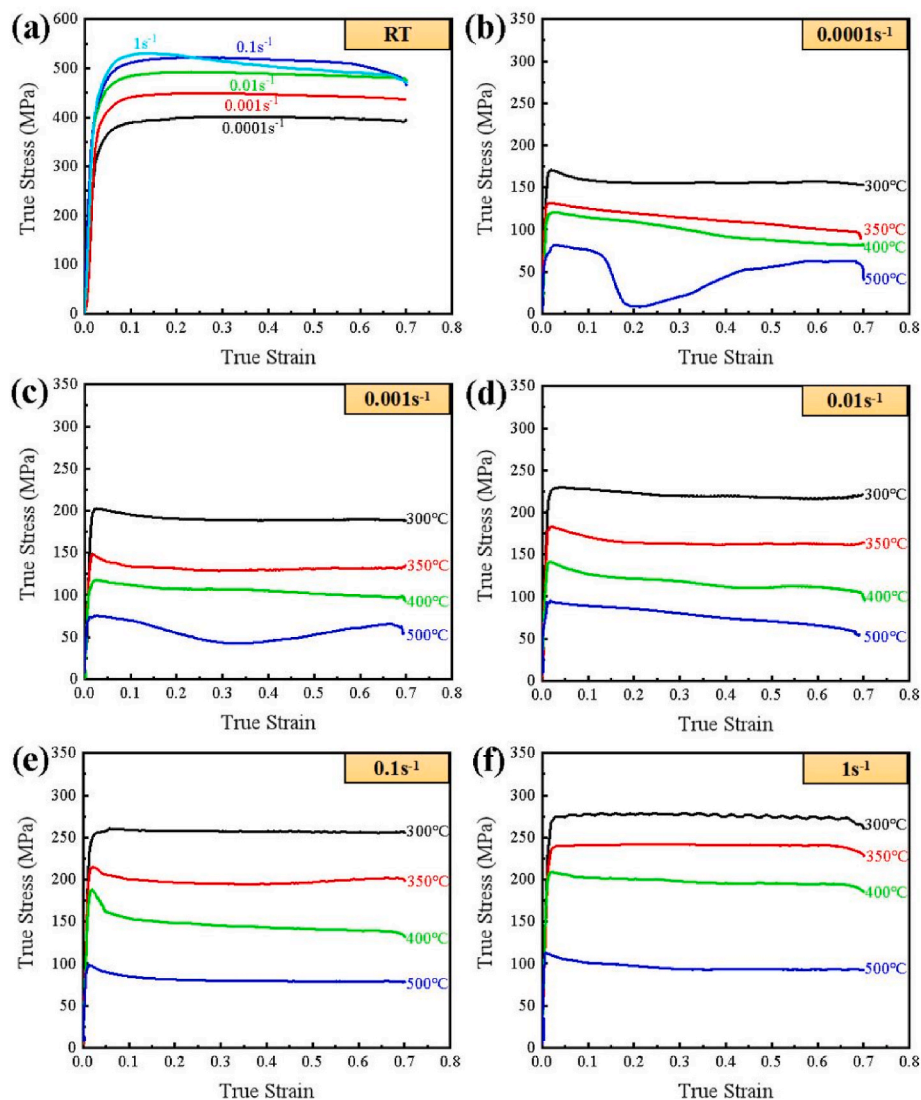
Fig. 2. True stress-strain curves of the 12.3% AlN$_p$/Al composite after compression deformation under different temperatures and strain rates: (a) RT; (b) 0.0001 s^{-1}; (c) 0.001 s^{-1}; (d) 0.01 s^{-1}; (d) 0.01 s^{-1}; (f) 1 s^{-1}.

system (Zeiss Auriga) and a transmission electron microscopy (TEM, FEI, Hillsboro, USA). Specimens for the SEM/EBSD characterization were prepared by mechanical polishing. The operation voltage for EBSD scanning was 15 kV, and the step size was 0.05–0.2 μm. Due to the limitation of angular precision, misorientation below 2° was not measured to avoid spurious boundaries. All EBSD data were analyzed using the Channel 5 software. Thin foils for TEM observations were ground into a thin sheet of ~25 μm thickness, and then polished by ion beam using Gatan 691 precision ion polishing system (PIPS).

The extruded rod was cut into multiple cylindrical specimens with a height of 9 mm and a diameter of 6 mm along the extrusion direction. Isothermal compression tests were carried out on a Gleeble 3500 thermal simulation tester under the room temperatures (RT), 300 °C, 350 °C, 400 °C and 500 °C with the strain rates of 0.0001 s^{-1}, 0.001 s^{-1}, 0.01 s^{-1}, 0.1 s^{-1} and 1 s^{-1}, respectively. Each compressed sample was heated to the target temperature at a heating rate of 10 °C/s and held for 5 min for uniform heating before isothermal compression. Both the indenter and the samples were coated with graphite lubricant to avoid the effect of friction during the test. The height of the deformed specimens was reduced to half of the initial height. After the isothermal compression, all specimens were rapidly quenched in water at room temperature.

3. Results

3.1. Microstructure of the extruded 12.3% AlN$_p$/Al composite before isothermal compression

The microstructure of the initial specimen before compression is shown in Fig. 1. As shown in Fig. 1a–b, the initial specimen formed a non-uniform microstructure along the extrusion direction, the particle-rich zone with the dispersive distribution of nanoparticles and the particle-lean zone with a α-Al stripe together constituted a layered heterogeneous structure. According to the EDS point analysis, the dispersively distributed nanoparticles were AlN. Fig. 1c–d shows the TEM images of the composite and it can be found that the fine AlN nanoparticles formed clusters around the Al grains, and the AlN clusters interconnected with each other to form a network structure (shown in the dashed line in Fig. 1d), which could effectively bear higher load at a high temperature.

In addition, Fig. 1e–g shows the EBSD analysis of the Al matrix grains. As shown in Fig. 1e, the high-angle grain boundaries (HAGBs, indicated by black lines) and low-angle grain boundaries (LAGBs, indicated by white lines) accounted for 59% and 13%, respectively. In particular, there was a region with similar grain color in the lower-left
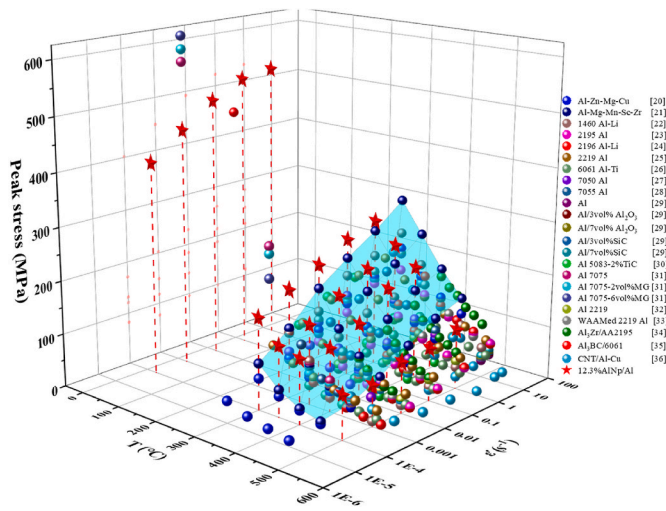
Fig. 3. Comparison of the hot compression properties of the 12.3% AlN$_p$/Al composites in this work with other reported high performance aluminum alloys [20–36].

corner, which was an α-Al stripes formed by the elongation of Al grains along the extrusion direction due to the hot extrusion process and lack of particles pinning (corresponding to the AlN-lean zone in Fig. 1a–b). They had similar grain orientations and exhibited preferred orientations to some extent. Meanwhile, the grain size of the 12.3% AlN$_p$/Al composite was 1.07 ± 0.17 μm and had a good uniformity (Fig. 1f). Fig. 1g shows that most of the initial specimens of the composite were substructure grains accompanied by a few recrystallized grains and very few deformed grains with the percentages of 72%, 19%, and 9%, respectively (Fig. 1h), which was mainly due to the occurrence of the DRV and DRX during the hot extrusion deformation.

3.2. Hot deformation behavior

Fig. 2 lists the true stress-strain curves for all specimens. As shown in Fig. 2a, the compressive strength of the 12.3% AlN$_p$/Al composite increased with the increase of strain rate at room temperature, from 402 MPa at 0.0001 s^{-1} to 531 MPa at 1 s^{-1}, which increased by 32.1%. The flow stress remained relatively constant with the increase of strain, and although a slight decrease occurred at 1s^{-1}, the flow stress at a strain of 0.69 remained at 88.7% of the peak stress. The high temperature true stress-strain curves for the 12.3% AlN$_p$/Al composite under different deformation temperatures and different strain rates are listed in Fig. 2b–4f. At 300 °C, 350 °C and 400 °C, the compressive strength increased from 171 MPa, 131 MPa, 121 MPa at 0.0001 s^{-1} to 279 MPa, 242 MPa and 209 MPa at 1 s^{-1}, an increase of 63%, 85% and 73% respectively. However, the corresponding compressive strength increased from 82 MPa at 0.0001 s^{-1} to 113 MPa at 1 s^{-1} under 500 °C, an increase of 37%. This is mainly because high strain rate means high speed of dislocation production, and the high temperature of 500 °C was favorable for annihilating the dislocations and occurring recrystallization. Similarly, with the strain increase, flow stress did not occur significantly reduction at high temperature deformation conditions, except for 500 °C/0.0001 s^{-1}, indicating that the 12.3% AlN$_p$/Al composite has good thermal stability during whole compression deformation. It is noticed that an abnormal fluctuation on the flow curve at 500 °C/0.0001 s^{-1}, which indicated that deformation instability occurred during the compressive deformation. It is supposed that the phenomena caused by the special heterogeneous structure of the 12.3% AlN$_p$/Al composite. The Al strips were prone to soften at high temperature and cracks tended to appear at the zone interfaces. At higher strain rates, a large number of dislocations were pinned by the AlN$_p$ at the interface thus preventing softening and crack extension. In addition, the network structure of AlN$_p$ in the AlN-rich zone further acted as work hardening, which balanced the softening effect at high temperature. At low strain rates, the rate of dislocation multiplication was slow, which reduced the suppression effect of the softening of the Al strips and the
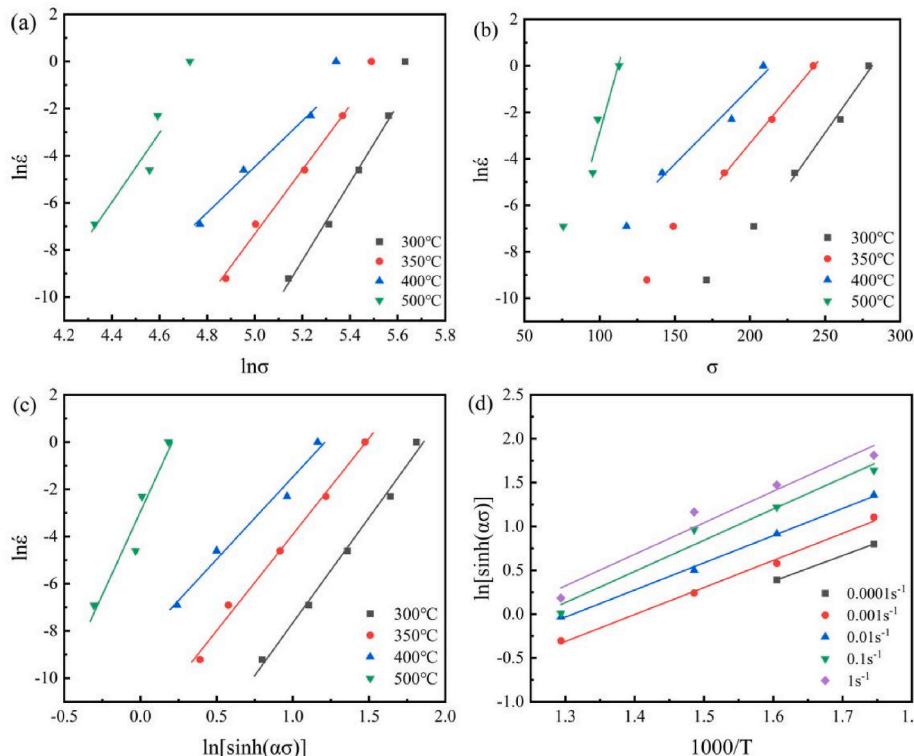
Fig. 4. linear fitting relationship under different conditions:(a) ln σ − lnε̇; (b) σ − lnε̇; (c) ln[sin h(ασ)] − lnε̇; (d) (1000 /T) − ln[sin h(ασ)].

Table 1
Peak stresses of different compression specimens.

Strain rate (s^{-1})	Peak stress(MPa)				
	25 °C	300 °C	350 °C	400 °C	500 °C
0.0001	402	171	131	121	82
0.001	449	203	149	118	76
0.01	492	230	183	142	95
0.1	522	260	215	188	98
1	531	279	242	209	113

Table 2
Types of dynamic softening mechanisms of the 12.3% AlN$_p$/Al composite under different deformation compression conditions (A:DRV, B: DRX).

Strain rate (s^{-1})	Temperature(°C)			
	300	350	400	500
0.0001	B	B	B	B
0.001	B	B	B	B
0.01	B	B	B	B
0.1	A	B	B	B
1	A	A	B	B

extension of cracks, resulting in deformation instability. However, the AlN-rich zone was the main microstructure the 12.3% AlN$_p$/Al composite, even if instability occurred, it was confined within the Al stripes, thus exhibiting a high peak stress at 500 °C/0.0001 s^{-1}. Peak stresses of compression tests under different deformation conditions were determined (in Table 1).

Fig. 3 shows the compressive properties of the 12.3% AlN$_p$/Al composite and other traditional high performance aluminum alloys. It can be seen that the compressive strength of the 12.3% AlN$_p$/Al composite at 300 °C could exceed 200 MPa and even reached at least 76 MPa at 500 °C, which exhibited higher room temperature and high temperature compressive properties than most other aluminum alloys. Among them, although there were a few aluminum alloys with higher room temperature compressive properties than the 12.3% AlN$_p$/Al composite, their compressive properties at high temperatures were lower than that of the 12.3% AlN$_p$/Al composite. This suggests that the aluminum alloys with excellent room temperature compressive properties often have difficulty in maintaining superior high temperature compressive properties, while the 12.3% AlN$_p$/Al composite in this work could maintain a high level of compressive properties at both room and high temperatures.

In addition, two shapes of the compression curves were found: at strain rates of 0.0001–0.1 s^{-1}, the curve rises first, then enters the stable stage, and finally decreases; at strain rates of 1 s^{-1}, the curve first rises to the highest point, then decreases, and finally enters the stable stage. These two curve shapes are defined as DRV and DRX shapes, respectively [20], and these curve features are more obvious at high temperatures. It indicated that the 12.3% AlN$_p$/Al composite exhibited different dynamic softening mechanisms at different deformation conditions (as in Table 2).

3.3. Constitutive equation

The constitutive equation is usually established to describe the relationship between flow stress, strain rate and deformation temperature in hot deformation. In this paper, the Arrhenius constitutive model has been adopted, which has three types of expressions according to the range of applicability, as follows [37]:

$$\dot{\varepsilon} = A_1 \sigma^{n_1} \exp\left(-\frac{Q}{RT}\right) \tag{1}$$
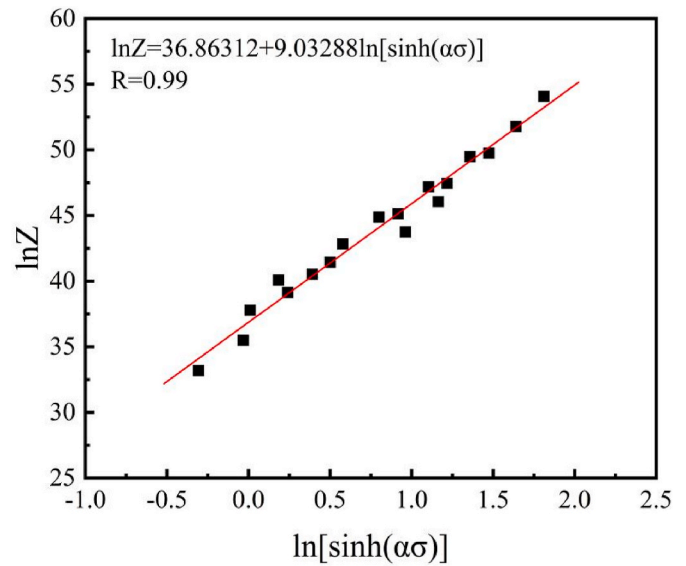
Fig. 5. Linear fitting relationship between the ln[sinh(ασ)] and Z-parameter lnZ.

$$\dot{\varepsilon} = A_2 \exp(\beta\sigma)\exp\left(-\frac{Q}{RT}\right) \tag{2}$$

$$\dot{\varepsilon} = A[\sinh(\alpha\sigma)]^n \exp\left(-\frac{Q}{RT}\right) \tag{3}$$

Where $\dot{\varepsilon}$ is the strain rate, Q is the activation energy of hot deformation, R is the ideal gas constant (R = 8.314 J/mol-K), T is the absolute temperature(K), A$_1$, A$_2$, A, n, n$_1$, α and β are the material constants, and α = β/n$_1$. Eq. (1) is applied to low stress levels (ασ < 0.8), Eq. (2) is applied to high stress levels (ασ > 1.2), and Eq. (3) is applied to all stress levels. To solve the equation, the above three equations are taken as logarithms on both sides, respectively, and collated to obtain:

$$\ln\dot{\varepsilon} = n_1 \ln \sigma + \ln A_1 - \frac{Q}{RT} \tag{4}$$

$$\ln\dot{\varepsilon} = \beta\sigma + \ln A_2 - \frac{Q}{RT} \tag{5}$$

$$\ln\dot{\varepsilon} = n \ln[\sinh(\alpha\sigma)] + \ln A - \frac{Q}{RT} \tag{6}$$

The linear relationship between the low strain levels (ln σ − ln$\dot{\varepsilon}$) and the high strain levels (σ − ln$\dot{\varepsilon}$) can be obtained from Eqs. (4) and (5), respectively, and the average values of n$_1$ = 13.65 and β = 0.1166 MPa^{-1} are obtained from the linear fit results shown in Fig. 4a–b, where the values of 400 °C/0.0001 s^{-1} and 500 °C/0.0001s^{-1} were removed as large deviation data. α = β/n$_1$ = 0.009 MPa^{-1}. The linear relationship of ln[sinh(ασ)] − ln$\dot{\varepsilon}$ can be obtained by substituting α = 0.009 MPa^{-1} into Eq. (6) and the average value of n = 9.539 obtained by linear fitting, as shown in Fig. 4c. According to Eq. (6):

$$Q = RnS$$

$$n = \left.\frac{\partial\ln\dot{\varepsilon}}{\partial\ln[\sinh(\alpha\sigma)]}\right|_T \tag{7}$$

$$S = \left.\frac{\partial\ln[\sinh(\alpha\sigma)]}{\partial(1/T)}\right|_{\dot{\varepsilon}}$$

Based on the above equation, there is a linear relationship between (1/T) and ln[sinh(ασ)], and S is the average slope of the liner fitting of (1/T) − ln[sinh(ασ)]. Fig. 4d is the relationship of (1000/T) − ln[sinh(ασ)], and the average slope of the liner fitting is 3.249, thus S =
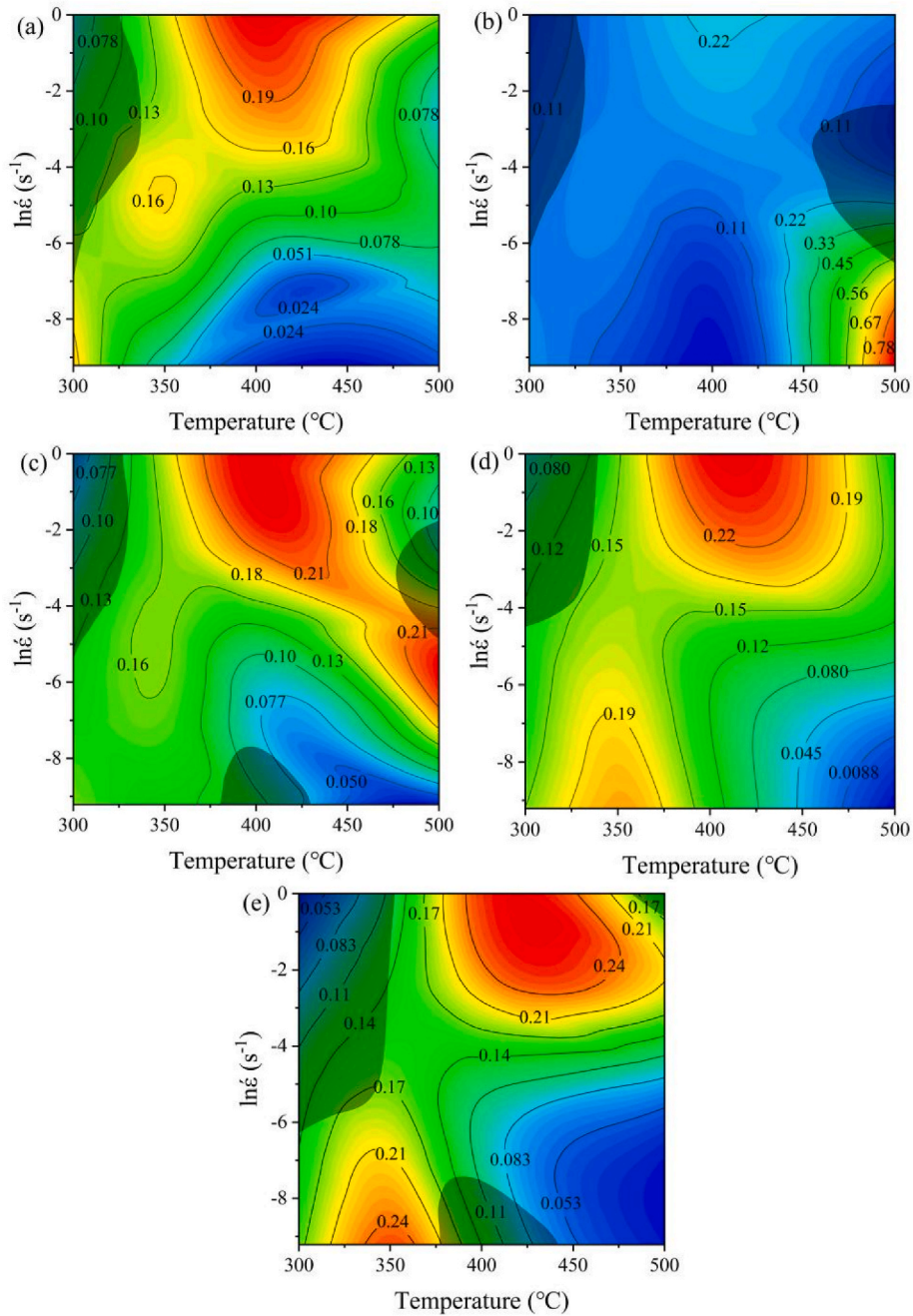
Fig. 6. Hot processing maps at different true strains: (a) 0.1; (b) 0.2; (c) 0.4; (d) 0.6; (e) 0.69.

3249. Therefore, Q is calculated as 257.67 kJ/mol. This is due to the pinning effect of the dispersively distributed AlN_p on the dislocations and the thermal stability of the AlN_p, which together prevented dislocation movement, resulting in a high Q value.

In addition, the relationship between the strain rate and the deformation temperature can be expressed by introducing the Zener-Hollomon parameter (Z-parameter) as [38]:

$$Z = \dot{\varepsilon} \exp\left(\frac{Q}{RT}\right) = A[\sin h(\alpha\sigma)]^n \tag{8}$$

$$\ln Z = \ln A + n[\sin h(\alpha\sigma)] \tag{9}$$

The $\ln[\sin h(\alpha\sigma)] - \ln Z$ image is plotted in Fig. 5, and the intercept of the linearly fitted line with the lnZ axis is A value, $A = 1.02 \times 10^{16}$.

In addition, the relationship between σ and Z parameter can be

further obtained by Eq. (10):

$$\sigma = \frac{1}{\alpha} \ln\left\{ \left(\frac{Z}{A}\right)^{1/n} + \left[\left(\frac{Z}{A}\right)^{2/n} + 1 \right]^{1/2} \right\} \tag{10}$$

In summary, by substituting all the required parameters into Eq. (3), Eq. (8), and Eq. (10), the Arrhenius flow stress relationship, the Z-parameter expression, and the constitutive equation between the σ and the Z-parameter can be expressed as:

$$\dot{\varepsilon} = 1.02 \times 10^{16} [\sin h(0.009\sigma)]^{9.03} \exp\left(-\frac{257670}{RT}\right) \tag{11}$$

$$Z = \dot{\varepsilon} \exp\left(\frac{257670}{RT}\right) \tag{12}$$
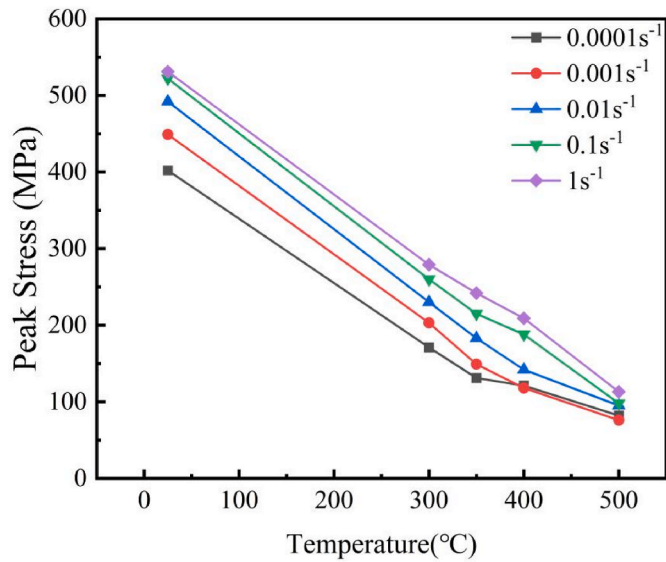
Fig. 7. Peak stresses for the 12.3% AlNp/Al composite under different deformation conditions.

$$\sigma = 111.11 \ln\left\{ \left(\frac{Z}{1.02 \times 10^{16}}\right)^{1/9.03} + \left[\left(\frac{Z}{1.02 \times 10^{16}}\right)^{2/9.03} + 1\right]^{1/2} \right\} \quad (13)$$

3.4. Hot processing map

Microscopic unstable phenomena such as localized flow, cracks, microscopic pores, and adiabatic shear bands occurred frequently during hot deformation [29,35]. Therefore, in addition to the processability of the composite, the evolution of the microstructure should be considered. In this paper, we establish hot processing maps based on Dynamic Material Model (DMM) to determine the optimal range of process parameters for the 12.3% AlNp/Al composite from both power dissipation and unstable deformation.

According to the power dissipation theory, the total dissipation P is divided into two parts [39]:

$$P = \sigma\dot{\varepsilon} = G + J = \int_0^{\dot{\varepsilon}} \sigma d\dot{\varepsilon} + \int_0^{\dot{\varepsilon}} \dot{\varepsilon} d\sigma \quad (14)$$

Where G is the plastic deformation dissipation power and J is the structural evolution dissipation power. At a certain deformation temperature and strain, the relationship between flow stress and strain rate can be expressed as $\sigma = K\dot{\varepsilon}^m$, where K is the material constant, and m is the strain rate sensitivity index, which is expressed as:

$$m = \left(\frac{\partial \ln \sigma}{\partial \ln \dot{\varepsilon}}\right)_{\varepsilon,T} \quad (15)$$

The structural evolution dissipation energy J can be expressed as:

$$J = \frac{m\sigma\dot{\varepsilon}}{1+m} \quad (16)$$

When $0 < m < 1$, the dissipation state is non-ideal linear, so the power dissipation efficiency η is introduced, which is expressed as:

$$\eta = \frac{J}{J_{max}} = \frac{2m}{1+m} \quad (17)$$

When the value of η is high, there are two deformation states of the material: better deformation performance and deformation instability. To determine the deformation state, the instability expression by Prasad established is derived as:

$$\xi(\dot{\varepsilon}) = \frac{\partial \ln\left(\frac{m}{1+m}\right)}{\partial \ln \dot{\varepsilon}} + m < 0 \quad (18)$$

According to the above equation, η and ξ are determined to build the hot processing maps, as shown in Fig. 6.

Except for the strain of 0.2, the power dissipation efficiency η is higher in the medium temperature and high strain rate region (380–450 °C, 0.04-1s^{-1}) of the 12.3% AlNp/Al composite, and the η increased from 0.19 to 0.24 with increasing strain, which means this region has better processability. The η in the low temperature and low strain rate region (320–370 °C, 0.0001–0.002s^{-1}) also gradually increases as the strain increases from 0.1 to 0.69, indicating that the processability in this region is more strain sensitive. However, the shaded part of the instability occurs mainly in the low temperature and high strain rate region (300–350 °C, 0.01–1 s^{-1}), and the area of the unstable region increases with increasing strain. It is indicated that flow instability tends to happen in this range, resulting in poor processability. The instability zone also varies with strain, which requires more strict control of the processing. In particular, the anomaly exhibited by the strain of 0.2 is related to the significant decrease in flow stress under 500 °C at a low strain rate in the compression curve, which is analyzed in detail below. In conclusion, combining all the hot processing maps and the corresponding unstable zones, the optimal processing range for the 12.3% AlNp/Al composite is about 380–450 °C and 0.04–1 s^{-1} strain rates, where the power dissipation efficiency is kept beyond 0.21.

4. Discussion

4.1. Effect of strain rate and deformation temperature on high temperature deformation behavior

As a reflection of the maximization of the work-hardening effect, peak flow stress is an important indicator of the hot deformation
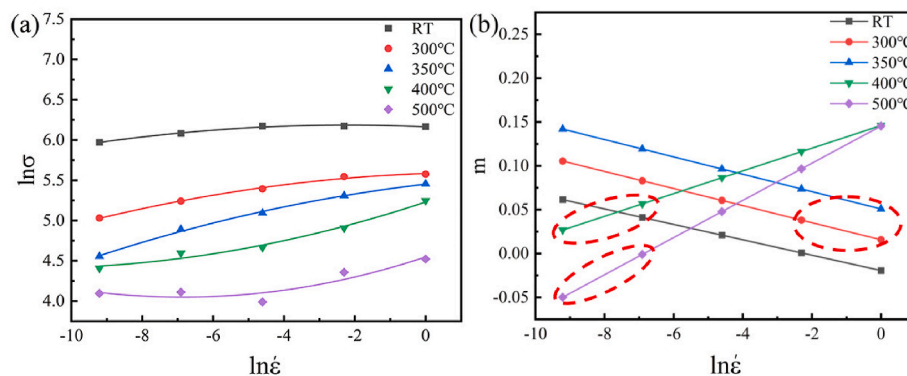
Fig. 8. (a) Relationship between the flow stress and strain rate under the strain of 0.69; (b) the m value for different conditions under the strain of 0.69.
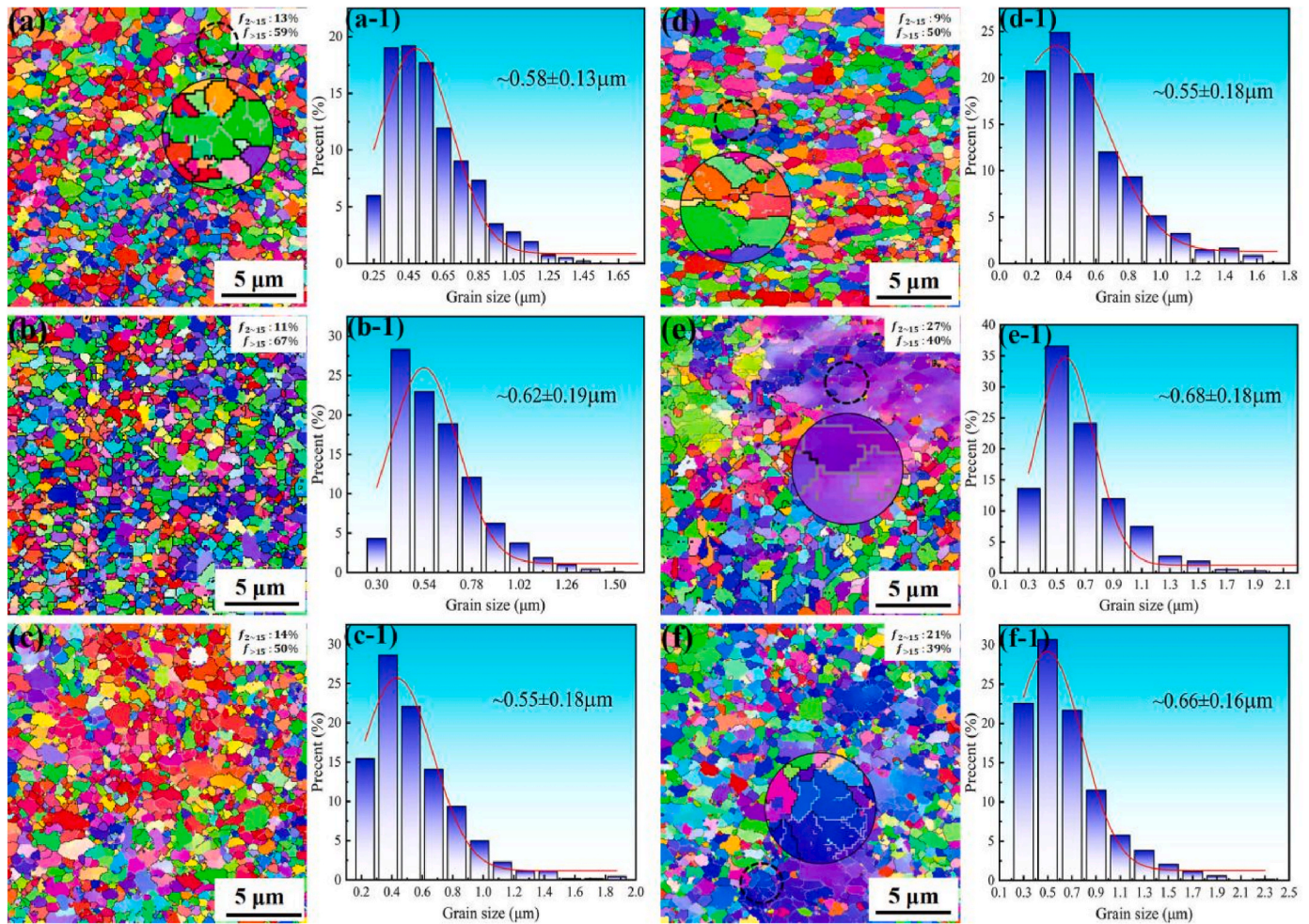
Fig. 9. EBSD maps and the corresponding grain size statistics of compression specimens under different deformation conditions: (a, b, c) 300 °C/0.0001 s^{-1}, 0.01 s^{-1}, 1 s^{-1}; (d, e, f) 500 °C/0.0001 s^{-1}, 0.01 s^{-1}, 1 s^{-1}.

properties of materials. The variation in peak flow stress is attributed to the competition between dynamic softening and work hardening in high temperature deformation. As shown in Fig. 7, the peak stresses of the 12.3% AlN$_p$/Al composite during high temperature compression deformation were related to the deformation temperature and strain rate. Although different types of curves occurred under different conditions, the peak stresses generally showed an increase with decreasing deformation temperature and increasing strain rate. This was mainly due to the significant influence of deformation temperature and strain rate on the work-hardening effect of high temperature deformation of the 12.3% AlN$_p$/Al composite. With the deformation temperature increases, the thermal activation of the composite increases, and dislocations tended to migrate, leading to a reduction in dislocation density. And the efficiency of dislocation generation decreases with the strain rate decreases, which also leads to a reduction in dislocation density. Both of these would lead to a weakening in the work hardening effect.

In particular, at 400–500 °C, the differences in peak stress between 0.0001 s^{-1} and 0.001 s^{-1} were very small, declaring that the stress sensitivity of the composite at lower strain rates was weak. To further investigate the dependence of the high temperature deformation of the 12.3% AlN$_p$/Al composite on the deformation temperature and the strain rate, the strain rate sensitivity exponent (m) was used to evaluate it. By analyzing the value of m at a given deformation condition, the evolution of the composite microstructure can be predicted [40]. Generally, the higher the m value, the better the ductility of the material. while the m value approaches zero or appears negative, indicating the possible existence of microscopic defects in the material [40,41]. From

the hot processing map, the power dissipation efficiency was highest and the processability was most sensitive at a strain of 0.69. Based on the true stress-strain curve, the flow stress value at a strain of 0.69 was obtained. To improve the accuracy, the correlation between $\ln \sigma$ and $\ln \dot{\varepsilon}$ was obtained according to Eq. (15) as shown in Fig. 8a, the m value for various conditions was shown in Fig. 8b. As shown in Fig. 8b, the m values showed two opposite trends at high temperature, low strain rate condition and low temperature and high strain rate condition. When the temperature was below 350 °C, the m value increased with increasing of temperature and decreasing of strain rate. When the temperature was above 350 °C, the m value decreased with increasing of temperature and decreasing of strain rate, with a negative value at 0.0001 s^{-1}. This was because that dislocations had enough energy and time to move at high temperatures and low strain rates, and the material appeared to soften excessively, resulting in instability or defects. Therefore, the simultaneous action of high deformation temperatures and low strain rates should be avoided during hot processing. Combined analysis of the variation of m values and hot processing map, we can predict that the instability or poor processability would happen in the specific range as shown by the red circles in Fig. 8b (400–500 °C, 0.0001–0.001 s^{-1} and 300–350 °C, 0.1–1 s^{-1}), and the hot processing map for 0.69 strain confirmed this prediction.

4.2. Microstructure evolution and deformation mechanism

The EBSD maps of the 12.3% AlN$_p$/Al composite samples under different hot deformation conditions with 300 °C/0.0001 s^{-1}, 0.01 s^{-1}, 1
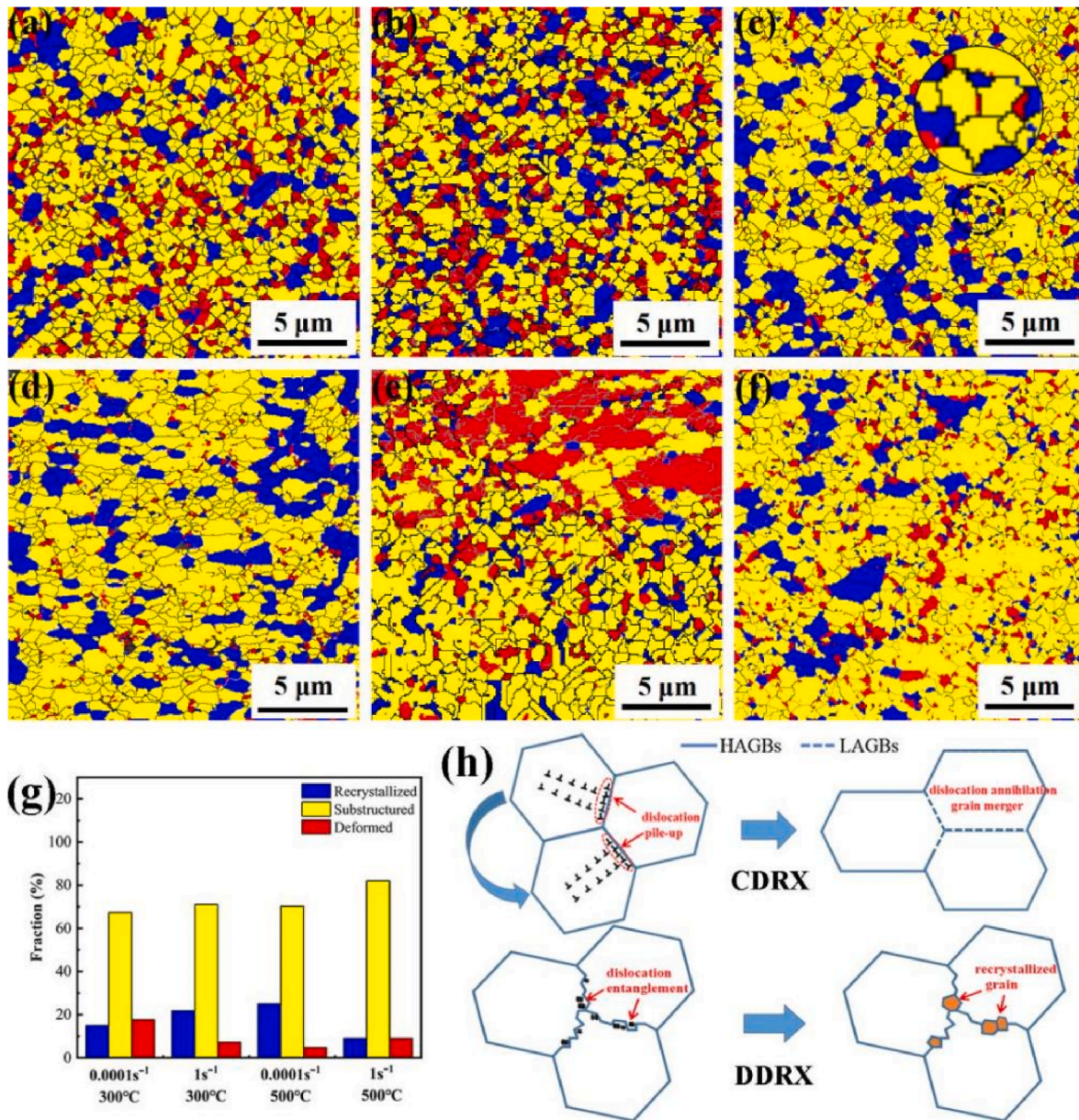
Fig. 10. Recrystallized distribution of compression specimens under different deformation conditions (blue is the recrystallized grain, yellow is the substructure grain, red is the deformed grain): (a, b, c) 300 °C/0.0001 s^{-1}, 0.01 s^{-1}, 1 s^{-1}; (d, e, f) 500 °C/0.0001 s^{-1}, 0.01 s^{-1}, 1 s^{-1};(g) Recrystallization statistics; (h)Scheme of deformation mechanism. (For interpretation of the references to color in this figure legend, the reader is referred to the Web version of this article.)

s^{-1} and 500 °C/0.0001 s^{-1}, 0.01 s^{-1}, 1 s^{-1} are shown in Fig. 9. The averaged grain sizes of all six high temperature compressed specimens were about 0.6 μm, which was reduced compared to the initial sample of ~1 μm. Based on the analysis of the compression curves, the composite did not cause matrix grain growth during hot compression deformation even though significant DRX occurred but instead promoted matrix grain refinement. This was due to the effective pinning of AlN$_p$ on dislocations at grain boundaries, which promoted DRX nucleation and inhibited grain growth, resulting in fine equiaxed grains in the particle-rich zone.

In addition, the matrix grains were obviously compressed after hot deformation, but from the local magnification, the compressed grains were composed of multiple small grains with similar colors, which had similar grain orientations (Fig. 9a–d). Meanwhile, coarse grains with similar grain orientation were observed in both Fig. 9e–f. These grains were connected with large segments of LAGBs and very small segments of HAGBs. According to the previous microstructure analysis, this region

was the AlN-lean zone, where small grains readily rotated to similarly oriented positions to form the coarse grains under the combined effect of DRX and loads at high temperatures. This also agrees well with the phenomenon that the proportion of LAGBs increased and the proportion of HAGBs decreased with increasing temperature and strain rate.

Three types of dynamic recrystallization have been reported: continuous dynamic recrystallization (CDRX), discontinuous dynamic recrystallization (DDRX), and geometric dynamic recrystallization (GDRX). CDRX is more likely to occur at high temperatures in the form of subgrain rotation, and DDRX is more likely to occur at high strain rates in the form of nucleation and growth [42]. As shown in Fig. 10, the microstructures of the specimens under different deformation conditions were dominated by substructures, and the volume fraction was not much different from the initial specimen. At the low strain rate of 0.0001s^{-1}, the pinning effect of AlN particles on grain boundary was still very strong at 300 °C, therefore the specimens showed more deformed grains. While the temperature rises to 500 °C, the DRX became easier,
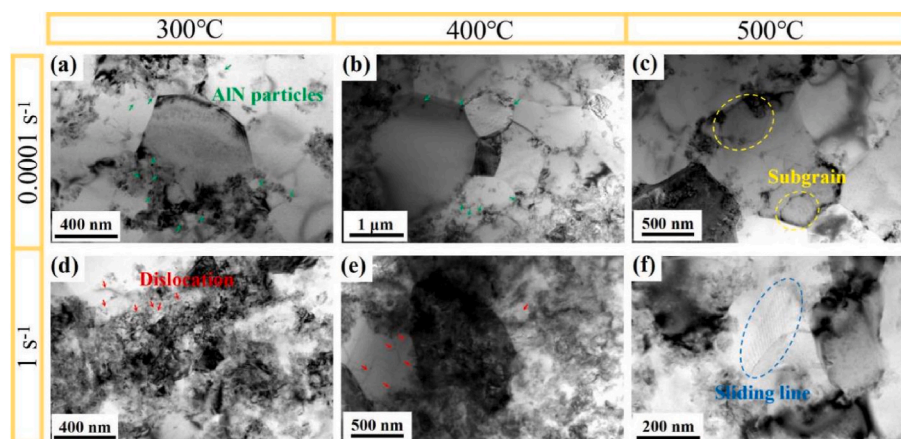
Fig. 11. TEM images of compressed specimens: (a–c) 0.0001 s^{-1}/300 °C,400 °C,500 °C; (d–f) 1 s^{-1}/300 °C,400 °C,500 °C.

the recrystallized grain fraction increased (Fig. 10g). As a continuation of DRV, DRX usually results from the transformation of LAGBs into HAGBs, and internal recrystallized grains are rotated from subgrains [43]. At a low strain rate, the dislocations had enough time to migrate and annihilate thus promoting DRV and grain rotation, which resulted in a reduction of poorly oriented grains and suborientation. This corresponded to the reduction of LAGBs and the increase of HAGBs in Fig. 9(a, d). At a high temperature of 500 °C, the pinning effect of AlN on the Al grains and dislocations was weakened, and enough thermal energy was beneficial to driving the growth subgrains, resulting in a maintenance of 50% HAGBs.

Comparing Fig. 10(a and c), the fraction of deformed grains decreased significantly with increasing strain rate at 300 °C, indicating that DRV occurred. While the fraction of recrystallized grains increased slightly, and the recrystallized grains were mainly distributed in serrated and bulging grain boundaries (Fig. 10c), which served as possible locations for recrystallization nucleation, thus indicating the presence of DDRX as well [44]. The presence of DDRX also explained the maintenance of more than half the proportion of the HAGBs as the strain rate increases at 300 °C (Fig. 9a–c). The wave shape of the flow stress curve at 300 °C/1 s^{-1} also confirms the occurrence of DDRX. The residual dislocations tangled and interacted with each other to form the dislocation cells, then gradually transformed into recrystallized grains. The nucleation and growth of recrystallized grains would promote the annihilation of dislocations [41]. Therefore, the deformation mechanism of hot deformation of the 12.3% AlN$_p$/Al composite at a low strain rate and the high temperature is CDRX, and the deformation mode is a rotation between individual grains or grain clusters. At a high strain rate and a low temperature, the deformation mechanism is dominated by DRV, accompanied by DDRX, and the deformation mode is dislocation entanglement form the substructure and nucleus at irregular grain boundaries (Fig. 10h).

In particular, an abnormally large area of deformed grains appeared in the 500 °C/0.01 s^{-1} (Fig. 10e), which is the AlN-lean zone. This indicated that the lack of AlN$_p$ pinning effect in this region caused more severe deformation. Gao et al. [45]. prepared an Al$_2$O$_3$/Al composite by in-situ and hot extrusion, which has a heterogeneous structure with alternating particle-lean zones and particle-rich zones, facilitating the mechanical properties. The 12.3% AlN$_p$/Al composite had a similar characteristic: the α-Al strips lacked AlN$_p$ distribution and AlN-rich zone formed a laminar heterogeneous structure. During the hot deformation, the α-Al stripes were prone to softening and cracking at high temperatures. In the AlN-rich zone, the presence of AlN$_p$ could prevent the softening and crack extension, thus limiting the instability to a few α-Al stripes and further improving the load-bearing capacity of the composite. This was the reason why there was a significant drop and rise of the flow stress at 500 °C/0.0001 s^{-1},0.001 s^{-1}. The unstable zone came from

the α-Al stripes, but the maintenance of peak stresses at high temperatures depends on these AlN nanoparticles.

As shown in Fig. 11, AlN$_p$ were distributed around the Al grains. On the one hand, the Al grains were expected to grow at high temperatures, but the pinning effect of AlN$_p$ on the grain boundaries prevented grain growth. Intragranular nanoparticles (within the interior of primary α-Al) formed NP layers at grain boundaries, which restricted the solute diffusion and hence inhibited the grain growth [46]. On the other hand, the AlN$_p$ distributed at the Al grain boundaries to form irregular boundaries, which prevented the softening of the grain boundaries. These two aspects together maintained the high temperature compressive strength of the 12.3% AlN$_p$/Al composite. At 300 °C, with the increased strain rate, dislocations were heavily accumulated in the AlN-rich zone and formed the dislocation walls with mutual pinning of AlN$_p$. This can divide the deformed grains into substructures, which was beneficial to DRV [47]. At low strain rates, with the increased temperature, most of the dislocations within the grains disappeared, the grain boundaries became clear. In addition, the sub-grains could be found within the grain, which was attributed to the rotation of the AlN$_p$ during deformation releasing accumulated dislocations and promoting CDRX. At high strain rates, when the deformation temperature increased to 500 °C, the pinning effect of dislocations was significantly weakened, and the slip lines appeared (Fig. 11i). This indicated that the pinning effect of AlN$_p$ on dislocations was reduced at high temperatures and that it was easier to promote the occurrence of dislocation sliding. This was the main reason for the compression strength had been reduced to 37% at 500 °C.

5. Conclusions

In this work, isothermal compression tests were carried out on a AlN$_p$/Al composite under room temperature and high temperature of 300–500 °C with strain rates of 0.0001–1 s^{-1}. The hot deformation behavior of the AlN$_p$/Al composite was systematically investigated. The conclusions are as follows.

(1) The AlN$_p$/Al composite had excellent and stable high temperature strength at room temperature and high temperature, especially the high temperature compressive strength was higher than most of traditional high-performance aluminum alloy. The flow stress was maintained more than 80% of the peak stress.

(2) Based on the experimental results, the Arrhenius flow stress relationship between the flow stress, the deformation temperature and strain rate of the 12.3% AlN$_p$/Al composite were calculated. According to the hot processing maps, the optimal hot processing range for the 12.3% AlN$_p$/Al composite was determined to be 380–450 °C and 0.04–1 s^{-1}.

(3) The dependence of the 12.3% AlN_p/Al composite on strain rate and deformation temperature was explored by the strain rate sensitivity exponent *m*. It was also found that *m* value could be effectively used to predict the instability region and the simultaneous action of high deformation temperature and high strain rate should be avoided during hot deformation.

(4) The hot deformation mechanism varied with the deformation conditions. At low temperature and high strain rate, DRV dominated the microstructure evolution, accompanied by DDRX formed by dislocation entanglement at irregular grain boundaries. At high temperature and low strain rate, rotation of the AlN_p released accumulated dislocations, leading to rotation between grains or grain clusters and grains merging, promoting the development of CDRX.

(5) The dislocation pinning effects and particle pinning effects induced by AlN_p in the matrix grains effectively prevented grain boundary softening and grain growth. At the same time, the special layered heterogeneous structure and network structure further inhabited the high temperature softening.

CRediT authorship contribution statement

Mengqi Jiang: Investigation, Writing – original draft, Writing – review & editing. **Yuli Wu:** Investigation. **Jinfeng Nie:** Conceptualization, Funding acquisition, Supervision, Writing – review & editing. **Yuyao Chen:** Formal analysis. **Yong Fan:** Formal analysis. **Xiangfa Liu:** Supervision. **Yonghao Zhao:** Supervision, Writing – review & editing.

Declaration of competing interest

The authors declare that they have no known competing financial interests or personal relationships that could have appeared to influence the work reported in this paper.

Data availability

Data will be made available on request.

Acknowledgements

References

[1] S. Senthil, M. Raguraman, D. Thamarai Manalan, Manufacturing processes & recent applications of aluminum metal matrix composite materials: a review, Mater. Today: Proc. 45 (2021) 5934–5938.

[2] W. Zhang, J. Xu, Advanced lightweight materials for Automobiles: a review, Mater. Des. 221 (2022), 110994.

[3] S. Deshmukh, G. Joshi, A. Ingle, D. Thakur, An overview of aluminum Matrix Composites: particulate reinforcements, manufacturing, modelling and machining, Mater. Today: Proc. 46 (2021) 8410–8416.

[4] S. Deshmukh, G. Joshi, A. Ingle, D. Thakur, An overview of aluminum Matrix Composites: particulate reinforcements, manufacturing, modelling and machining, Mater. Today: Proc. 46 (2021) 8410–8416.

[5] P. Garg, A. Jamwal, D. Kumar, K.K. Sadasivuni, C.M. Hussain, P. Gupta, Advance research progresses in aluminum matrix composites: manufacturing & applications, J. Mater. Res. Technol. 8 (5) (2019) 4924–4939.

[6] J.F. Nie, Y. Fang, L. Zhao, X.F. Liu, Y.H. Zhao, Latest research progress on the strengthening and toughening mechanism of particle reinforced aluminum matrix composites, Mater. Rep. 35 (9) (2021) 9009–9015.

[7] G. Yi, H. Li, C.Y. Zang, W.L. Xiao, C.L. Ma, Remarkable improvement in strength and ductility of Al-Cu foundry alloy by submicron-sized TiC particles, Mater. Sci. Eng., A 855 (2022), 143903.

[8] X.R. Yan, K. Zhao, K.W. Xie, M.X. Han, G.L. Liu, X.F. Liu, Microstructure evolution, mechanical properties and strengthening mechanisms in the hot extruded Si_3N_4 particle reinforced Al-Cu-Mg composite, Mater. Sci. Eng., A 850 (2022), 143516.

[9] S.S. Tang, S.Y. Shao, H.Y. Liu, F.L. Jiang, D.F. Fu, H. Zhang, J. Teng, Microstructure and mechanical behaviors of 6061 Al matrix hybrid composites reinforced with SiC and stainless steel particles, Mater. Sci. Eng., A 804 (2021), 140732.

[10] J.F. Nie, Y.Y. Chen, X. Chen, X.F. Liu, G.L. Liu, Y.H. Zhao, Y.T. Zhu, Stiff, strong and ductile heterostructured aluminum composites reinforced with oriented nanoplatelets, Scripta Mater. 189 (2020) 140–144.

[11] P.H. Ye, X.C. Jin, W.B. Fang, X.W. Li, H. Wu, G.H. Fan, Hot deformation behavior and microstructure evolution of a high Nb containing PM TiAl composite reinforced with Ti_2AlC particles, Mater. Today Commun. 29 (2021), 102862.

[12] Y.Q. Ning, T. Wang, M.W. Fu, M.Z. Li, L. Wang, C.D. Zhao, Competition between work-hardening effect and dynamic-softening behavior for processing as-cast GH4720Li superalloys with original dendrite microstructure during moderate-speed hot compression, Mater. Sci. Eng., A 642 (2015) 187–193.

[13] K.K. Alaneme, S.A. Babalola, M.O. Bodunrin, On the prediction of hot deformation mechanisms and workability in Al6063/Ni_p and Al6063/$steel_p$ composites using hyperbolic-sine constitutive equation, Mater. Today: Proc. 38 (2021) 942–948.

[14] Y.H. Bian, T. Gao, G.L. Liu, X. Ma, Y.Y. Ren, X.F. Liu, Design of an in-situ multi-scale particles reinforced (Al_2O_3+ZrB_2+AlN)/Al composite with high strength, elasticity modulus and thermal stability, Mater. Sci. Eng., A 775 (2020), 138983.

[15] L. Cao, B. Chen, J. Wan, K. Kondoh, B. Guo, J. Shen, J.S. Li, Superior high-temperature tensile properties of aluminum matrix composites reinforced with carbon nanotubes, Carbon 191 (2022) 403–414.

[16] L.Y. Huang, Y.T. Zhao, X.Z. Kai, C. Guan, X. Gao, P.F. Zhao, T. Wang, Research on high strength and creep behavior of in-situ (Al_2O_3+ZrB_2)/7055 Al nanocomposites, Mater. Char. 193 (2022), 112296.

[17] D. Gong, L.T. Jiang, J.T. Guan, K. Liu, Z.H. Yu, G.H. Wu, Stable second phase: the key to high-temperature creep performance of particle reinforced aluminum matrix composite, Mater. Sci. Eng., A 770 (2020), 138551.

[18] M. Balog, P. Krizik, J. Dvorak, O. Bajana, J. Krajcovic, M. Drienovsky, Industrially fabricated in-situ Al-AlN metal matrix composites (part B): the mechanical, creep, and thermal properties, J. Alloys Compd. 909 (2022), 164720.

[19] X. Ma, Y.F. Zhao, W.J. Tian, Z. Qian, H.W. Chen, Y.Y. Wu, X.F. Liu, A novel Al matrix composite reinforced by nano-AlN_p network, Sci. Rep. 6 (1) (2016), 34919.

[20] J.H. Zhao, Y.L. Deng, J.G. Tang, J. Zhang, Influence of strain rate on hot deformation behavior and recrystallization behavior under isothermal compression of Al-Zn-Mg-Cu alloy, J. Alloys Compd. 809 (2019), 151788.

[21] J.Y. Jiang, F. Jiang, H.F. Huang, M.H. Zhang, Z.Q. Tang, M.M. Tong, Hot deformation analysis and microstructure evolution of Al-Mg-Mn-Sc-Zr alloy by isothermal compression, J. Alloys Compd. 858 (2021), 157655.

[22] S. Xiang, D.Y. Liu, R.H. Zhu, J.F. Li, Y.L. Chen, X.H. Zhang, Hot deformation behavior and microstructure evolution of 1460 Al-Li alloy, Trans. Nonferrous Metals Soc. China 25 (12) (2015) 3855–3864.

[23] J.J. Zhang, Y.P. Yi, S.Q. Huang, X.C. Mao, H.L. He, J.G. Tang, W.F. Guo, F. Dong, Dynamic recrystallization mechanisms of 2195 aluminum alloy during medium/high temperature compression deformation, Mater. Sci. Eng., A 804 (2021), 140650.

[24] X.X. Chen, G.Q. Zhao, X.T. Zhao, Y.X. Wang, X. Xu, C.S. Zhang, Constitutive modeling and microstructure characterization of 2196 Al-Li alloy in various hot deformation conditions, J. Manuf. Process. 59 (2020) 326–342.

[25] H.L. He, Y.P. Yi, J.D. Cui, S.Q. Huang, Hot deformation characteristics and processing parameter optimization of 2219 Al alloy using constitutive equation and processing map, Vacuum 160 (2019) 293–302.

[26] W. Chen, Y.P. Guan, Z.H. Wang, Hot deformation behavior of high Ti 6061 Al alloy, Trans. Nonferrous Metals Soc. China 26 (2) (2016) 369–377.

[27] Y. Deng, Z.M. Yin, J.W. Huang, Hot deformation behavior and microstructural evolution of homogenized 7050 aluminum alloy during compression at elevated temperature, Mater. Sci. Eng., A 528 (3) (2011) 1780–1786.

[28] J. Ren, R.C. Wang, Y. Feng, C.Q. Peng, Z.Y. Cai, Hot deformation behavior and microstructural evolution of as-quenched 7055 Al alloy fabricated by powder hot extrusion, Mater. Char. 156 (2019), 109833.

[29] K.C. Nayak, P.P. Date, Hot deformation flow behavior of powder metallurgy based Al-SiC and Al-Al_2O_3 composite in a single step and two-step uni-axial compression, Mater. Char. 151 (2019) 563–581.

[30] V. Senthilkumar, A. Balaji, R. Narayanasamy, Analysis of hot deformation behavior of Al 5083-TiC nanocomposite using constitutive and dynamic material models, Mater. Des. 37 (2012) 102–110.

[31] M.S. Xie, C. Suryanarayana, Y.L. Zhao, W.W. Zhang, C. Yang, G.Q. Zhang, Y.N. Fu, Z. Wang, Abnormal hot deformation behavior in a metallic-glass-reinforced Al-7075 composite, Mater. Sci. Eng., A 785 (2020), 139212.

[32] L. Liu, Y.X. Wu, H. Gong, F. Dong, A.S. Ahmad, Modified kinetic model for describing continuous dynamic recrystallization behavior of Al 2219 alloy during hot deformation process, J. Alloys Compd. 817 (2020), 153301.

[33] Y.H. Zhou, X. Lin, N. Kang, Z.N. Wang, H. Tan, W.D. Huang, Hot deformation induced microstructural evolution in local-heterogeneous wire + arc additive manufactured 2219 Al alloy, J. Alloys Compd. 865 (2021), 158949.

[34] Q.B. Yang, Y.J. Deng, M. Yang, Z.Q. Zhang, W.G. Li, Q. Liu, Effect of Al_3Zr particles on hot-compression behavior and processing map for Al-Cu-Li based alloys at elevated temperatures, Trans. Nonferrous Metals Soc. China 30 (4) (2020) 872–882.

[35] Y.F. Zhao, A.S.S. Singaravelu, X. Ma, Q.D. Zhang, X.F. Liu, N. Chawla, Micromechanical properties and deformation behavior of Al_3BC/6061 Al composites via micropillar compression, Mater. Sci. Eng., A 773 (2020), 138852.

[36] C.H. Li, R.S. Qiu, B.F. Luan, W.J. He, Z.Q. Li, Hot deformation and processing maps of as-sintered CNT/Al-Cu composites fabricated by flake powder metallurgy, Trans. Nonferrous Metals Soc. China 28 (9) (2018) 1695–1704.

[37] N. Raja, B.S.S. Daniel, Microstructural evolution of Al-7.3Zn-2.2Mg-2Cu (Al7068) alloy in T6 condition during isothermal compression using 3-dimensional processing map, J. Alloys Compd. 902 (2022), 163690.

[38] L.L. Chang, L.W. Zheng, Isothermal compression behavior and constitutive modeling of Ti-5Al-5Mo-5V-1Cr-1Fe alloy, Trans. Nonferrous Metals Soc. China 28 (6) (2018) 1114–1122.

[39] H. Mohammadi, A.R. Eivani, S.H. Seyedein, M. Ghosh, H.R. Jafarian, An investigation of hot deformation behavior of Zn-22Al alloy and development of its processing maps during isothermal compression, J. Mater. Res. Technol. 14 (2021) 507–520.

[40] Y. Sun, Z.P. Wan, L.X. Hu, J.S. Ren, Characterization of hot processing parameters of powder metallurgy TiAl-based alloy based on the activation energy map and processing map, Mater. Des. 86 (2015) 922–932.

[41] Y.Y. Chen, M.Q. Li, L. Li, Kinetic variables based constitutive model for high temperature deformation of Ti-46.5Al-2Nb-2Cr, J. Mater. Res. Technol. 15 (2021) 3525–3537.

[42] Y. Zhang, J. Jiang, Y. Wang, Y. Liu, M. Huang, Hot deformation behavior and microstructure evolution of hot-extruded 6A02 aluminum alloy, Mater. Char. 188 (2022), 111908.

[43] Y. Zhang, J.F. Jiang, Y. Wang, G.F. Xiao, Y.Z. Liu, M.J. Huang, Recrystallization process of hot-extruded 6A02 aluminum alloy in solid and semi-solid temperature ranges, J. Alloys Compd. 893 (2022), 162311.

[44] X.X. Wang, M. Zhan, P.F. Gao, P.Y. Ma, K. Yang, Y.D. Lei, Z.X. Li, Deformation mode dependent mechanism and kinetics of dynamic recrystallization in hot working of titanium alloy, Mater. Sci. Eng., A 772 (2020), 138804.

[45] T. Gao, L.Y. Liu, J.P. Song, G.L. Liu, X.F. Liu, Synthesis and characterization of an in-situ Al_2O_3/Al-Cu composite with a heterogeneous structure, J. Alloys Compd. 868 (2021), 159283.

[46] K. Wang, H.Y. Jiang, Y.W. Jia, H. Zhou, Q.D. Wang, B. Ye, W.J. Ding, Nanoparticle-inhibited growth of primary aluminum in Al-10Si alloys, Acta Mater. 103 (2016) 252–263.

[47] Z.Y. Chen, R.Q. Lu, S.W. Zheng, J. Tang, F.L. Jiang, L. Deng, L. Huang, J. Teng, Microstructural characteristics and deformation behaviors of an Al-Mg-Si alloy with improved strength and conductivity processed by continuous casting and expansion extrusion, J. Mater. Res. Technol. 22 (2023) 445–460.